Reversible writing of high mobility and high carrier density doping patterns in two-dimensional van der Waals heterostructures

Wu Shi[1,2,3], Salman Kahn[1,2,3], Lili Jiang[1,2,3], Sheng-Yu Wang[1,2,3], Hsin-Zon Tsai[1,2,3], Dillon Wong[1,2,3], Takashi Taniguchi[4], Kenji Watanabe[4], Feng Wang[1,2,3], Michael Crommie[1,2,3], Alex Zettl[1,2,3,*]

[1]Department of Physics, University of California, Berkeley, California 94720, USA

[2]Materials Sciences Division, Lawrence Berkeley National Laboratory, Berkeley, California 94720, USA

[3]Kavli Energy NanoSciences Institute at the University of California and the Lawrence Berkeley National Laboratory, Berkeley, California 94720, USA

[4]National Institute for Materials Science, 1-1 Namiki, Tsukuba 305-0044, Japan

*Correspondence to: azettl@berkeley.edu

A key feature of two-dimensional materials is that the sign and concentration of their carriers can be externally controlled with techniques such as electrostatic gating. However, conventional electrostatic gating has limitations, including a maximum carrier density set by the dielectric breakdown, and ionic liquid gating and direct chemical doping also suffer from drawbacks. Here, we show that an electron-beam doping technique can be used to reversibly write high-resolution doping patterns in hexagonal boron nitride encapsulated graphene and molybdenum disulfide (MoS_2) van der Waals heterostructures. The MoS_2 device exhibits an order of magnitude decrease of subthreshold swing after doping,

24 **whereas the doped graphene devices demonstrate a previously inaccessible regime**
25 **of high carrier concentration and high mobility, even at room temperature. We also**
26 **show that the approach can be used to write high-quality p-n junctions and**
27 **nanoscale doping patterns, illustrating that the technique can create nanoscale**
28 **circuitry in van der Waals heterostructures.**

29

30 Externally controlled modulation of charge density is at the heart of the
31 semiconductor electronics industry[1]. Modulation via traditional electrostatic gating has
32 been shown to be effective for two-dimensional (2D) materials[2,3], but fundamental
33 challenges remain in achieving ultra-high carrier concentration beyond the dielectric
34 breakdown limit and in precisely defining local charge modulation with a nanoscale
35 spatial resolution[4–8]. Although alternative doping methods such as electrolyte gating and
36 chemical intercalation[9–12] are capable of inducing high carrier densities, they inevitably
37 introduce disorder and unintentional electrochemical reactions which degrade device
38 mobility[13,14]. Additionally, these methods are not suitable for local charge modulation
39 and realistic commercial device implementation. Other techniques, such as using
40 lithographically defined gates[4–8] or molecular self-assemblies on surfaces[15,16], can
41 achieve impressive spatially controlled charge doping, but they cannot achieve
42 simultaneous high carrier concentrations. They face additional limitations in applications
43 that require rewritability or complex circuit designs.

44 Recent developments in van der Waals (vdW) heterostructures have led to alternate
45 approaches to doping/gating that do not require complex processing masks or resists,
46 with possible high mobility and high carrier concentration. For example, photo-induced

47 doping and doping using voltage pulses from the tip of a scanning tunneling microscope
48 (STM) have been demonstrated[17,18]. Both methods operate by activating defects within a
49 hexagonal boron nitride (BN) layer[19] that electrostatically influences the adjacent
50 graphene layer. While intriguing, these methods suffer from limited spatial resolution or
51 cannot be scaled to the mesoscopic lengths. Some attempts have also been made to
52 achieve n- and p-doping in graphene and other two-dimensional materials via more
53 flexible electron-beam (e-beam) irradiation using a scanning electron microscope
54 (SEM)[20–24]. The focused e-beam also enables direct writing of doping patterns into a
55 single graphene layer[20,22,23]. However, these efforts have faced common challenges
56 including unstable doped states, inevitable degradation of device quality, and limited
57 controllability of doping concentrations[20–24].

58 In this Article, we report a fully reversible e-beam doping scheme for graphene and
59 MoS_2 vdW heterostructures. We employ a BN encapsulated device geometry, which
60 protects the 2D materials from direct e-beam irradiation[25] and enables non-volatile
61 doping that is further controlled by a back-gate electric field. With this approach, we can
62 precisely tune the carrier density in the 2D materials in pre-selected spatially defined
63 regions with nanoscale resolution. The doping regions persist even after the e-beam and
64 back-gate voltage are removed, and are entirely rewritable. Importantly, we achieve high
65 electron and hole carrier densities beyond $\pm 10^{13}$ cm^{-2} in a single back-gate
66 BN/graphene/BN heterostructure device while maintaining ultra-high room-temperature
67 mobility at the theoretical phonon-scattering limit[26]. We also realize similar doping
68 effects in MoS_2 device with decreased subthreshold swing (SS) compared with the device
69 before doping.

70

71 ## Electron beam doping scheme and electrical measurements

72 The experimental scheme for the combined e-beam/back-gate doping technique is
73 illustrated in Fig. 1 (see Methods). Doping is performed in a standard SEM with electrical
74 feedthroughs, which allow for *in-situ* transport measurements. All graphene and MoS_2
75 devices are encapsulated by BN layers. This avoids depositing contaminants or e-beam
76 induced reactions on the graphene or MoS_2 surface which can introduce disorder and
77 degrade mobility[25]. The heterostructure is in vacuum at room temperature and the SEM-
78 generated e-beam, with energy ranging from 1 keV to 30 keV, is used for exposure.

79 Figs. 1b, c illustrates the e-beam induced doping effect in graphene. The graphene
80 device is initially largely undoped and its charge neutral point (CNP) V_{CNP} is close to 0 V.
81 With applied V_G = 30 V the device resistance R drops from 1.2 kΩ at the CNP to 180 Ω
82 as the back-gate field moves the device off of the CNP. At time t = 10 s (Fig. 1b), the 1
83 keV SEM e-beam is turned on and scanned over the entire device (see Methods) while V_G
84 is maintained at the preset voltage V_{SET} = 30 V. As Fig. 1b shows, within several seconds
85 R increases (also see Supplementary Note 5 and Fig. S6) and saturates near ~1.4 kΩ,
86 close to the pre-doped CNP resistance of 1.2 kΩ. At t = 40 s the e-beam is blanked, but R
87 remains locked and high at 1.4 kΩ; the device is now stably doped. As shown in Fig. 1c,
88 the CNP has been shifted by 30V after exposure, equal to V_{SET} applied during the doping
89 process. The same doping process is also applicable to MoS_2 transistor devices, as shown
90 in Fig. 1d, e, f. The monolayer (ML) MoS_2 device is initially electron doped with a
91 threshold voltage V_{TH} = -33 V. After a 1 keV e-beam exposure at V_{SET} = 0 V (Fig. 1e),
92 the V_{TH} is shifted to 0 V (Fig.1f). The graphene retains a very high field-effect mobility of

93 ~ 5 x 10^4 $cm^2V^{-1}s^{-1}$, and the MoS_2 also retains a high mobility of ~ 130 $cm^2V^{-1}s^{-1}$ at room
94 temperature. Notably, the graphene response curve after doping is even slightly sharper
95 than the initial curve (Fig.1c) and the subthreshold swing of the MoS_2 device is one order
96 of magnitude smaller after e-beam doping (see Supplementary Note 3 and Fig. S3 - S4),
97 indicating an overall reduction of charge inhomogeneity in the devices.
98

99 **Gate bias and energy dependence of electron-beam induced doping**

100 By employing different V_{SET} values during the doping process, pre-selected doping
101 levels can be "written" into the device. The process can be applied multiple times (with
102 different V_{SET}) to the same device and is fully reversible. Fig. 2a and 2b show
103 respectively the transport characteristics of the same graphene and MoS_2 devices after
104 successive doping with a 1 keV e-beam with different V_{SET}, respectively. The 1 keV e-
105 beam induced doping causes a shift of the CNP (ΔV_{CNP}) or threshold voltage (ΔV_{TH}) close
106 to the V_{SET} value both for electron and hole doping with the polarity controlled by V_{SET}.
107 Remarkably, all transfer curves preserve the same sharp features, indicating little device
108 degradation even after multiple exposures with a 1 keV e-beam. This is in clear contrast
109 to previous e-beam doping reports that all showed inevitable mobility degradation[20–24].
110 Notably, our e-beam doping does not cause a 2*H* to 1*T* phase transition[27,28] in MoS_2 (see
111 Supplementary Note 18 and Fig. S27) due to the low dosage exposure and BN
112 encapsulation, in contrast to previous reports[20].
113 The e-beam doping process is sensitive to the e-beam energy. Even for the same
114 device, doping achieved using an e-beam energy of 30 keV is qualitatively different than
115 that obtained using an e-beam energy of 1 keV, suggesting different mechanisms behind

116 doping with a 1 keV beam versus a 30 keV beam. Figs. 2c and 2d show the transport
117 properties of the same graphene and MoS_2 devices after 30 keV e-beam induced doping
118 with different V_{SET}. Hysteresis and leakage current measurements are presented in SI
119 (Supplementary Note 6 and Figs. S13 - S14). Here, for a given V_{SET}, we observe an
120 opposite doping effect in Fig. 2c compared to the 1 keV case in Fig. 2a. When a positive
121 V_{SET} is applied, the graphene CNP shifts to a negative value, corresponding to *n*-doping
122 (whereas a positive V_{SET} leads to *p*-doping in the 1 keV case). Moreover, the CNP is
123 shifted to a much larger value than $|V_{SET}|$, indicating a higher doping concentration
124 induced using a 30 keV e-beam doping than for the 1 keV case. For 30 keV e-beam
125 doping, the field-effect mobility shows a slight doping dependence, but the sample still
126 achieves a remarkably high room-temperature mobility, with $\mu_{FET} \approx 3 \times 10^4$ $cm^2V^{-1}s^{-1}$ for
127 a doping concentration of $\pm 5 \times 10^{12}$ cm^{-2} (Supplementary Note 2 and Fig. S2). 30 keV e-
128 beam doping can induce highly doped states even beyond $\pm 1 \times 10^{13}$ cm^{-2} with relatively
129 small V_{SET} values. For example, as shown in Fig. 2c, the graphene device can be highly
130 doped and the CNP moved far beyond -80 V for V_{SET} = 30 V. Fig. 2d shows a similar
131 doping effect in MoS_2 for the 30 keV e-beam exposure. A highly electron-doped state is
132 achieved for V_{SET} = 30 V (red curve in Fig. 2d), the opposite of what occurs in the 1 keV
133 case (Fig. 2b). We also observed a reduction of the field-effect mobility for V_{SET} = -45 V,
134 which further indicates that high-energy e-beam exposure causes doping in devices
135 through a different mechanism than low-energy e-beam exposure. We note that the e-
136 beam induced doping effects are reproducible and repeatable in multiple devices and for
137 multiple cycles (Supplementary Note 1, Note 7, Fig. S1 and Fig. S15). Moreover, the

138 doped device is quite stable even in an ambient environment (Supplementary Note 5 and
139 Figs. S7 - S12).
140

141 Electrical characterization of highly doped devices

142 Next, we focus on the BN/Gr/BN heterostructure and characterize the device
143 performance after e-beam induced doping. We employ Hall effect measurements to
144 determine explicitly the doping concentrations and mobilities for both highly *n*- and *p*-
145 doped states (Supplementary Note 4 and Fig. S5). For 30 keV e-beam doping, the doping
146 concentration easily reaches ~1.7×10^{13} cm^{-2} for *n*-doping and ~ -1×10^{13} cm^{-2} for *p*-
147 doping. Such high carrier concentrations cannot typically be achieved with conventional
148 SiO_2 back-gated devices, as the required back-gate voltage would greatly exceed the
149 breakdown voltage of the BN/SiO_2 dielectric. Fig. 3a shows the Hall mobility μ_{Hall} as a
150 function of carrier density n_{Hall} for both *n*- and *p*-doped devices induced by 30 keV e-
151 beam doping. The Hall mobility at 300 K is close to 10^4 $cm^2V^{-1}s^{-1}$ for a doping
152 concentration of 1.7×10^{13} cm^{-2}, comparable to the acoustic-phonon-limited mobility
153 predicted for intrinsic graphene[26,29,30] (Supplementary Note 10). The room-temperature
154 mobility reported here in the high carrier density regime beyond $\pm 5 \times 10^{12}$ cm^{-2} (outside
155 the shaded region in Fig. 3a) is much higher than in other reports, even five times higher
156 than the mobility accessed by ionic liquid gating[10], electrolyte gating[9] and lithium
157 intercalation[12] on monolayer graphene devices (Fig. 3a).
158 In the high carrier density regime, the four-terminal sheet resistivity ρ for our
159 devices is ~40 ohms per square (Fig. 3b) at 300 K, comparable to the record sheet
160 resistivity for graphene[9,30]. As shown in Fig. 3b, ρ decreases monotonically with

161 temperature for both electron and hole-doped devices, showing metallic behavior. It
162 follows a linear T dependence in the high-temperature regime (30 K < T < 160 K) and
163 saturates to a very low residual resistance in the low-temperature limit[9,12,30]. This reflects
164 the cleanness of our device even in the high-density regime. Fig. 3c shows well-defined
165 Shubinikov-de Haas (SdH) oscillations in the same electron-doped device at temperature
166 2 K with a carrier density n_{SdH} of 1.28 x 10^{13} cm^{-2}, consistent with n_{Hall}. The Hall effect
167 mobility at 2 K reaches 10^5 $cm^2V^{-1}s^{-1}$. This reflects a homogeneous, high density, ultra-
168 high mobility two-dimensional electron gas (2DEG) in our device.
169

170 **Direct electron-beam writing of nanoscale doping patterns**

171 The e-beam activation process enables the writing of spatially complex doping
172 patterns with high resolution in a single vdW heterostructure device, without the need for
173 complex gating electrodes, ionic fluids, or deposition of foreign chemical species. By
174 using the lithography function in the SEM, the electron beam can be positioned to
175 different target regions and thereby be used to draw arbitrary patterns with nanoscale
176 precision. Here we demonstrate the creation of a high-quality graphene p-n junction by e-
177 beam induced doping. As shown in the inset of Fig. 3d, we use the lithography mode of
178 the SEM to selectively expose the region enclosed by the red rectangle and the blue
179 rectangle to a 2 keV e-beam while holding V_{SET} to ~ -20 V and 20 V, respectively. These
180 two regions thus respectively become electron and hole doped. Two distinct sharp peaks
181 are observed when measuring electrical resistance across the whole device, showing a
182 separation of the CNP of ~ 40 V. This is the clear characteristic feature of a high-quality
183 graphene p-n junction, vastly superior to those obtained in previous reports[15,17,23]. The p-n

184 junction is further investigated at low temperature. While in the quantum Hall regime,
185 there are three distinct regions that can be tuned into with the global back-gate: p-p, p-n
186 and n-n. Fig. 3e shows the longitudinal resistance across the p-n junction while varying
187 the magnetic field and the carrier density. In the p-n junction region, the longitudinal
188 resistance jumps into an insulating state due to the quantum Hall edge states
189 counterpropagating and interfering with each other[4,15]. While in the p-p region and n-n
190 region, there are edge states that propagate in the same direction and mix in the channel
191 as manifested in the Landau fan diagram. This proves our technique preserves the high
192 mobility of the device after patterning and can be used to engineer quantum states.
193 Moreover, it is highly reconfigurable and a p-i-n junction is also created after erasing the
194 previously written p-n junction in the same device (Supplementary Note 7 and Fig. S16).
195 The lithography mode of the SEM allows the writing of more sophisticated doping
196 patterns at high spatial resolution down to 200 nm. We use scattering-type scanning near-
197 field optical microscopy (s-SNOM) and electrostatic force microscopy (EFM) to image
198 some of the patterns we have created (see Methods). Figs. 3f and 3g show s-SNOM
199 images of a stripe pattern and a letter "B" pattern drawn using the e-beam lithography
200 mode with V_{SET} = 55 V and a beam energy of 2 keV (see dosage parameters in SI). The s-
201 SNOM image clearly reveals a striped doping modulation (Supplementary Note 8 and
202 Fig. S17) resulting from different scattering amplitudes of the infrared light in response to
203 different local carrier densities. The letter "B" pattern has a line width of ~ 200 nm, a
204 significant improvement over previous results[17,19]. This spatial resolution is confirmed
205 with our EFM measurement (Supplementary Note 9 and Fig. S18). We remark that our

intrinsic doping line width may be even smaller, since our EFM analysis neglects line charge electric field divergence.

Proposed doping mechanism

We now turn to the e-beam energy-dependent doping mechanism. It is revealing to plot the normalized effective capacitance $\Delta V_{\mathrm{CNP}}/V_{\mathrm{SET}}$ and $\Delta V_{\mathrm{TH}}/V_{\mathrm{SET}}$ vs V_{SET} (proportional to the electric field) for the graphene and MoS_2 devices as shown in Fig. 4a and 4b, respectively. For low beam energy (1 keV) exposures, $\Delta V_{\mathrm{CNP}}/V_{\mathrm{SET}}$ and $\Delta V_{\mathrm{TH}}/V_{\mathrm{SET}}$ remain nearly constant at unity, independent of V_{SET}. For higher beam energy (>> 1 keV) exposures, $\Delta V_{\mathrm{CNP}}/V_{\mathrm{SET}}$ and $\Delta V_{\mathrm{TH}}/V_{\mathrm{SET}}$ are strongly dependent on V_{SET} and the e-beam energy. Doping with a 30 keV exposure results in an effective capacitance is more than four times higher than the dielectric capacitance for electron doping. This indicates an electric-field and irradiation boosted charge accumulation process. MoS_2 exhibits an asymmetric behavior and here it is more difficult to access hole conduction compared to graphene, possibly because MoS_2 has a large band gap and the device is intrinsically electron doped. Nevertheless, the similar energy and electric field dependence of the doping effects suggests a general doping mechanism for our e-beam doping process in vdW heterostructures.

Here we propose a preliminary model for the doping mechanism but a full quantitative understanding requires further experimental and theoretical study. During e-beam exposure of the vdW heterostructures, there are a variety of processes occurring (secondary electron emission, plasmon decay, etc.)[31] but the primary effects that contribute to the doping are electron-hole pair generation and trap states in the

229 dielectrics[32]. Taking graphene as an example, for low e-beam energy (1 keV and 2 keV),
230 the electron beam primarily excites electron-hole pairs in bottom BN layers (see
231 Supplementary Note 12 and Fig. S20), i.e., the e-beam penetration depth, d_p, is smaller
232 than the BN thickness d_{BN} (Fig. 4c). For the case when $V_{SET} > 0$, hot electrons drift
233 towards the silicon due to the gate electric field E applied by V_{SET} but are trapped in BN
234 defects near the BN/SiO_2 interface. When there is enough charge in the BN trap states to
235 screen the gate electric field, the charging process stops and the graphene becomes charge
236 neutral at V_{SET} after e-beam exposure, as shown in Fig. 4c (top panel).

237 For high energy e-beam exposure (30 keV), electron-hole pairs are generated in both
238 the bottom BN and SiO_2 ($d_p >> d_{BN}$, also see Supplementary Fig. S20), whereupon they
239 separate due to the electric field E. With $V_{SET} > 0$, electron traps are activated in the BN
240 near the BN/SiO_2 interface while hole traps are activated in the SiO_2 near the BN/SiO_2
241 interface. These charged traps reduce the potential drop but the total applied potential
242 drop must equal V_{SET}, therefore more charge is accumulated in the dielectrics until an
243 equilibrium distribution is reached. Since the SiO_2 layer is much thicker and has a higher
244 defect density than the BN layer[19], more holes are trapped in SiO_2 than are electrons in
245 BN as shown in Fig. 4c. Consequently, the combined doping effects of activated defects
246 is opposite for a high (30 keV) vs. low (1 keV) energy e-beam. More control experiments
247 and detailed discussion of the proposed mechanism are included in the SI (Supplementary
248 Notes 11 - 14 and Figs. S19 - S23). This model can be also applied to MoS_2 to account
249 for the similar energy-dependent reversed doping effects, but admittedly further
250 development of the model is required to explain all subtleties of the doping behavior, for
251 example asymmetries in p- and n-type doping behavior.

Conclusions

We have reported an e-beam doping technique for BN encapsulated van der Waals heterostructures. The technique provides a reversible method to write complex and non-volatile doping patterns with high spatial resolution, high carrier density, and high mobility, even at room temperature. We demonstrate this by directly writing p–n junctions and nanoscale patterns, as well as achieving electron and hole carrier densities beyond $\pm 10^{13}$ cm^{-2} with high mobility in a BN/graphene/BN heterostructure device. We also show similar controlled doping in MoS_2 devices. Our method provides a route to create multi-component nanoscale circuitry in vdW heterostructures with minimal processing. It may also be an ideal approach to pattern superlattice potentials or customize the electronic properties of 2D materials for novel scientific studies and device applications.

Methods

Device fabrication:

High quality BN crystals from Taniguchi and Watanabe are exfoliated onto 285 nm SiO_2/Si substrates. We use BN flakes ranging in thickness from 8 - 40 nm for the top and bottom encapsulating layers. The BN encapsulated graphene and MoS_2 van der Waals heterostructures are fabricated using the dry pick-up transfer technique[30] and then annealed in an Ar/H_2 forming gas for 3 hours at 350 ^{o}C. The top BN layer is mandatory for high mobility devices as it prevents environmental surface contamination from reaching the critical graphene layer (Supplementary Note 15 and Fig. S24). Standard

275 electron-beam lithography processes are used to pattern etching masks and electrodes
276 onto the heterostructures. The thickness information for all the devices is provided in the
277 SI (Supplementary Note 17, Table S1 and Fig. S25).
278
279 **E-beam doping process:**
280 The heterostructure device is mounted in a SEM (model: FEI XL30 Sirion) using a
281 custom holder attached to an electrical feedthrough for doping and limited in-situ
282 transport measurement (Supplementary Note 17 and Fig. S26). We use a standard ac
283 voltage bias lock-in technique at 97.13 Hz to measure transport properties of the device
284 in the SEM chamber under a vacuum of 3 x 10^{-6} mbar at room temperature. Electron
285 beam energies range from 1 keV to 30 keV with beam current I_e ranging from 1 pA to 15
286 pA used for the e-beam induced doping.
287 Both normal scanning mode and lithography mode are implemented to study the
288 doping effect and write pre-designed doping patterns on the BN encapsulated graphene
289 and MoS_2 devices. For e-beam irradiation in the normal scanning mode, the exposed area
290 S is about 300 μm^2 including the whole heterostructure region. Resistance is monitored
291 during exposure and the exposure stopped when the irradiation induced resistance change
292 has stabilized. Typical exposure time t ranges from 30 seconds to 120 seconds. The
293 accumulated irradiation dosage D is given by $D = I_e t/Se$. For example, I = 10 pA, S = 300
294 μm^2, t = 60 seconds, then D = 200 $\mu C/cm^2$ (i.e., 12.5 e^-/nm^2). Once the resistance is
295 stabilized under a certain preset voltage V_{SET} during irradiation, additional exposure will
296 not cause further resistance changes. For lithography mode, we tested different dosage

parameters. To achieve high spatial resolution, a smaller dosage parameter is beneficial (Supplementary Notes 8 - 9 and Figs. S17 - S18).

Low-temperature transport measurements are performed in a Quantum Design PPMS after quickly transferring the doped sample from the SEM without significant exposure to ambient light (see Supplementary Note 5 and Fig. S12).

Near-field nano-imaging:

We employ a scattering-type scanning near-field optical microscope (s-SNOM) to obtain the near-field images of the samples. The s-SNOM is based on a tapping mode AFM. An infrared light beam (λ=10.6 μm) is focused onto the apex of a conductive AFM tip. An MCT detector placed in the far field is used to collect the scattered light, which carries local optical information of the sample. Near-field images are recorded simultaneously with the topographic information during the measurements. The optical contrast of doped and un-doped areas in the near-field images stem from their different local carrier densities, which result in different scattering amplitudes of the infrared light.

Data availability

The data that support the plots within this paper and other findings of this study are available from the corresponding author upon reasonable request.

References

1. Hu, C. *Modern semiconductor devices for integrated circuits*. (Pearson, 2010).

2. Novoselov, K. S. *et al.* Electric field effect in atomically thin carbon films. *Science*

320 **306**, 666–669 (2004).

321 3. Lui, C. H., Li, Z., Mak, K. F., Cappelluti, E. & Heinz, T. F. Observation of an
322 electrically tunable band gap in trilayer graphene. *Nat. Phys.* **7**, 944–947 (2011).

323 4. Williams, J. R., DiCarlo, L. & Marcus, C. M. Quantum Hall effect in a graphene p-
324 n junction. *Science* **317**, 638–641 (2007).

325 5. Özyilmaz, B. *et al.* Electronic transport and quantum hall effect in bipolar
326 graphene p-n-p junctions. *Phys. Rev. Lett.* **99**, 2–5 (2007).

327 6. Huard, B. *et al.* Transport measurements across a tunable potential barrier in
328 graphene. *Phys. Rev. Lett.* **98**, 8–11 (2007).

329 7. Liu, G., Velasco, J., Bao, W. & Lau, C. N. Fabrication of graphene p-n-p junctions
330 with contactless top gates. *Appl. Phys. Lett.* **92**, 1–4 (2008).

331 8. Dubey, S. *et al.* Tunable superlattice in graphene to control the number of dirac
332 points. *Nano Lett.* **13**, 3990–3995 (2013).

333 9. Efetov, D. K. & Kim, P. Controlling electron-phonon interactions in graphene at
334 ultrahigh carrier densities. *Phys. Rev. Lett.* **105**, 2–5 (2010).

335 10. Ye, J. *et al.* Accessing the transport properties of graphene and its multilayers at
336 high carrier density. *PNAS* **108**, 13002–13006 (2011).

337 11. Shi, W. *et al.* Superconductivity series in transition metal dichalcogenides by ionic
338 gating. *Sci. Rep.* **5**, 1–10 (2015).

339 12. Zhao, S. Y. F. *et al.* Controlled electrochemical intercalation of graphene/ h-BN
340 van der Waals heterostructures. *Nano Lett.* **18**, 460–466 (2018).

341 13. Xia, Y., Xie, W., Ruden, P. P. & Frisbie, C. D. Carrier localization on surfaces of
342 organic semiconductors gated with electrolytes. *Phys. Rev. Lett.* **105**, 36802

343 (2010).

344 14. Ovchinnikov, D. *et al.* Disorder engineering and conductivity dome in ReS2 with
345 electrolyte gating. *Nat. Commun.* **7**, 1–7 (2016).

346 15. Lohmann, T., Von Klitzing, K. & Smet, J. H. Four-terminal magneto-transport in
347 graphene p-n junctions created by spatially selective doping. *Nano Lett.* **9**, 1973–
348 1979 (2009).

349 16. Ojeda-Aristizabal, C. *et al.* Molecular arrangement and charge transfer in
350 C60/graphene heterostructures. *ACS Nano* **11**, 4686–4693 (2017).

351 17. Ju, L. *et al.* Photoinduced doping in heterostructures of graphene and boron nitride.
352 *Nat. Nanotechnol.* **9**, 348–352 (2014).

353 18. Velasco, J. *et al.* Nanoscale control of rewriteable doping patterns in pristine
354 graphene/boron nitride heterostructures. *Nano Lett.* **16**, 1620–1625 (2016).

355 19. Wong, D. *et al.* Characterization and manipulation of individual defects in
356 insulating hexagonal boron nitride using scanning tunnelling microscopy. *Nat.*
357 *Nanotechnol.* **10**, 949–953 (2015).

358 20. Zhou, Y. *et al.* Programmable graphene doping via electron beam irradiation.
359 *Nanoscale* **9**, 8657–8664 (2017).

360 21. Childres, I. *et al.* Effect of electron-beam irradiation on graphene field effect
361 devices. *Appl. Phys. Lett.* **97**, 173109 (2010).

362 22. Yu, X., Shen, Y., Liu, T., Wu, T. & Jie Wang, Q. Photocurrent generation in
363 lateral graphene p-n junction created by electron-beam irradiation. *Sci. Rep.* **5**, 1–8
364 (2015).

365 23. Iqbal, M. Z., Anwar, N., Siddique, S., Iqbal, M. W. & Hussain, T. Formation of

366 pn-junction with stable n-doping in graphene field effect transistors using e-beam
367 irradiation. *Opt. Mater.* **69**, 254–258 (2017).
368 24. Stará, V., Procházka, P., Mareček, D., Šikola, T. & Čechal, J. Ambipolar remote
369 graphene doping by low-energy electron beam irradiation. *Nanoscale* **10**, 17520–
370 17524 (2018).
371 25. Teweldebrhan, D. & Balandin, A. A. Modification of graphene properties due to
372 electron-beam irradiation. *Appl. Phys. Lett.* **94**, 92–95 (2009).
373 26. Hwang, E. H. & Sarma, S. Das. Acoustic phonon scattering limited carrier
374 mobility in two-dimensional extrinsic graphene. *Phys. Rev. Lett.* **77**, 1–6 (2008).
375 27. Katagiri, Y. *et al.* Gate-tunable atomically thin lateral MoS_2 Schottky junction
376 patterned by electron beam. *Nano Lett.* **16**, 3788–3794 (2016).
377 28. Xie, X. *et al.* Designing artificial 2D crystals with site and size controlled quantum
378 dots. *Sci. Rep.* **7**, 1–7 (2017).
379 29. Sule, N. & Knezevic, I. Phonon-limited electron mobility in graphene calculated
380 using tight-binding Bloch waves. *J. Appl. Phys.* **112**, 053702 (2012).
381 30. Wang, L. *et al.* One-dimensional electrical contact to a two-dimensional material.
382 *Science* **342**, 614–617 (2013).
383 31. Ausman, G. A. & McLean, F. B. Electron-hole pair creation energy in SiO_2. *Appl.*
384 *Phys. Lett.* **26**, 173–175 (1975).
385 32. Curtis, O. L., Srour, J. R. & Chiu, K. Y. Hole and electron transport in SiO_2 films.
386 *J. Appl. Phys.* **45**, 4506–4513 (1974).
387

388 **Acknowledgements:**

This work was supported in part by the Director, Office of Science, Office of Basic Energy Sciences, Materials Sciences and Engineering Division, and Molecular Foundry of the U.S. Department of Energy under Contract No. DE-AC02-05-CH11231, primarily within the van der Waals Heterostructures Program (KCWF16) which provided for development of the concept and device fabrication, e-beam doping, and transport characterization, and within the sp2-Bonded Materials Program (KC2207) which provided for s-SNOM measurements; and by the National Science Foundation, under Grant No.1542741 which provided for AFM topography and SdH measurements, and under Grant No.1807233 which provided for EFM measurements.

Author contributions:

A.Z., M.C., W.S., S.K., H.-Z.T., D.W. conceived the experiment. S.K., W.S. and S.-Y. W. contributed to device fabrication. W.S. and S.K. performed all electrical measurements, EFM measurements, and data analysis. K.W. and T.T. provided the BN crystals. L.L.J. and F.W. contributed to the s-SNOM measurement. W.S., S.K. and A.Z. co-wrote the manuscript with inputs and comments from all authors.

Competing interests:

The authors declare no competing interests.

Figures

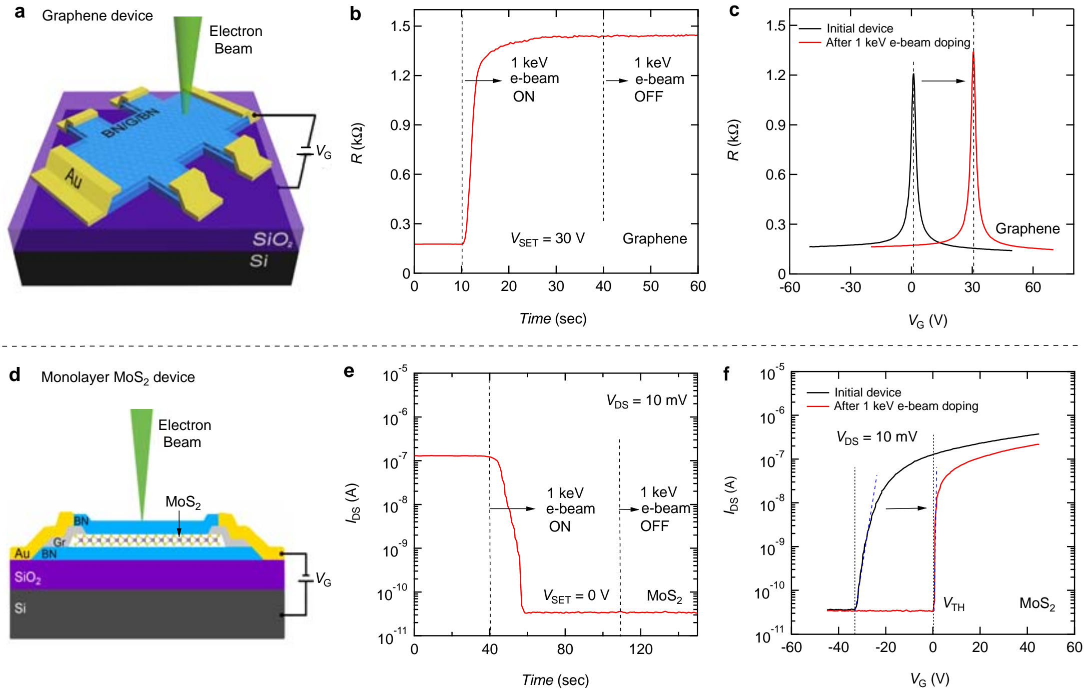

410

411 **Figure 1 | E-beam induced doping effect in graphene and MoS_2 van der Waals**

412 **heterostructures. a**, Experimental scheme for e-beam induced doping in graphene

413 device. Charge doping is induced in BN/Gr/BN by exposing it to a scanning electron

414 beam (1-30 keV) in a standard SEM for a few seconds while holding the back-gate

415 voltage $V_G \neq 0$ V. **b**, Resistance change of monolayer (ML) graphene (Device #1) when

416 a 1 keV e-beam is switched on and off (controlled by beam blanker in the SEM) with V_G

417 set to 30 V. V_{DS} = 50 µV for the graphene measurements. **c**, Transfer curves $R(V_G)$ of the

418 ML graphene before and after e-beam exposure. The CNP value is shifted from 0 V to 30

419 V (=V_{SET}), and the graphene has become uniformly hole doped. **d**, Cross-sectional view

420 of experimental scheme for e-beam doping in BN encapsulated ML MoS_2 transistor

421 device with multilayer graphene contacts. **e**, Source-drain current I_{DS} change of ML

422 MoS_2 when a 1 keV e-beam is switched on and off with V_G set to 0 V. **f**, $I_{DS}(V_G)$ of ML

423 MoS_2 before and after e-beam exposure. The threshold voltage V_{TH} is shifted from -33 V

424 to 0 V (=V_{SET}), and the calculated subthreshold swing (SS) decreases more than one order

425 of magnitude after doping (see Fig. S4).

426

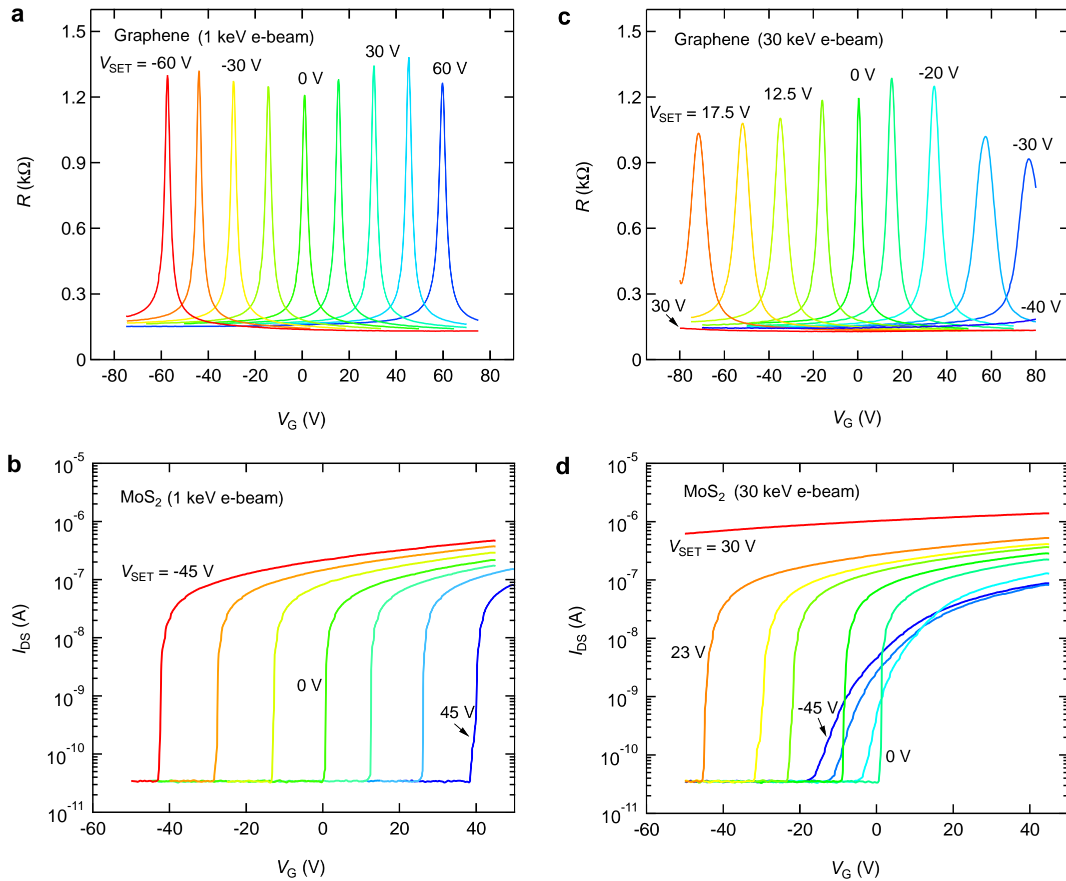

427

428 **Figure 2 | Energy dependence of e-beam induced doping effect in graphene and**

429 **MoS_2 van der Waals heterostructures. a**, Transfer curves $R(V_G)$ of graphene following

430 successive e-beam-induced doping using an e-beam energy of 1 keV. V_{SET} = -60, -45, -

431 30, -15, 0, 15, 30, 45, 60 V, respectively (from red to blue). **b**, $I_{DS}(V_G)$ of ML MoS_2 after

432 e-beam exposure using an e-beam energy of 1 keV. V_{SET} = -45, -30, -15, 0, 15, 30, 45,

433 respectively (from red to blue). V_{DS} = 10 mV for the MoS_2 measurements. **c**, Same as in **a**

434 but using a beam energy of 30 keV. V_{SET} = 30, 17.5, 15, 12.5, 10, 0, -10, -20, -25, -30, -

435 40 V, respectively (from red to blue). **d**, Same as in **b** but using a beam energy of 30 keV.

436 V_{SET} = 30, 23, 22, 21, 20, 0, -15, -30, -45 V, respectively (from red to blue).

437

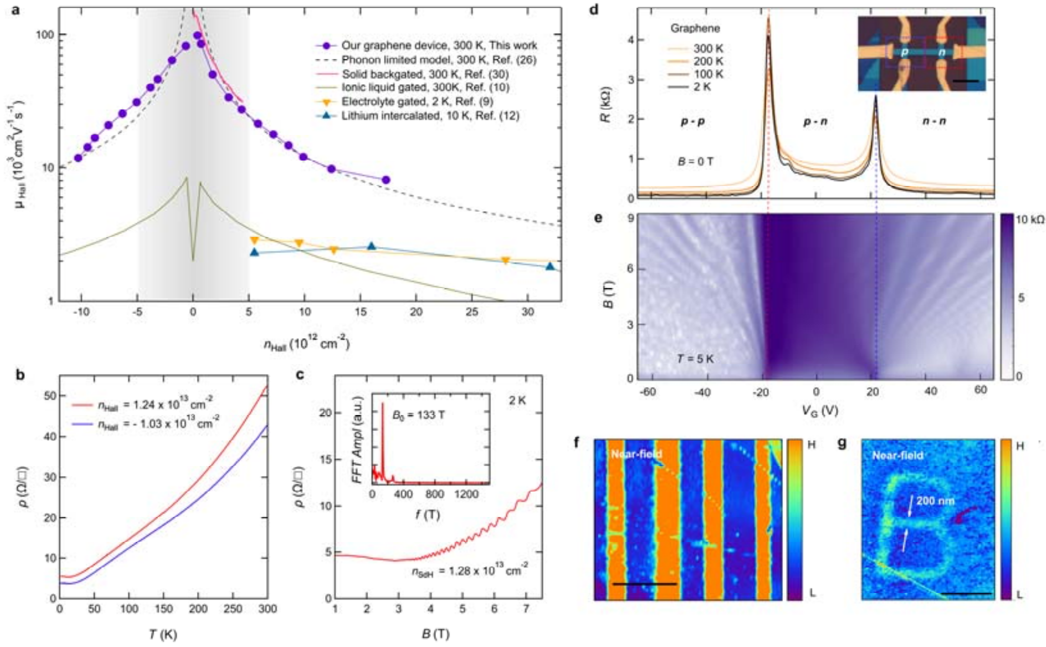

438

439 **Figure 3 | Transport characteristics and spatially controlled nanoscale doping**

440 **patterns of BN/Gr/BN heterostructures by e-beam induced doping. a**, Hall effect

441 mobility vs carrier density for 30 keV e-beam doped monolayer (ML) graphene samples

442 at 300 K compared to other highly doped ML graphene samples reported in literature.

443 Grey shaded region indicates conventional back-gate accessible carrier density regime. **b**,

444 Four-terminal sheet resistivity ρ of 30 keV e-beam highly electron and hole-doped ML

445 graphene devices, showing metallic behavior. **c**, ρ of electron-doped device in **b**

446 measured as a function of magnetic field B at 2 K, showing well-defined periodic SdH

447 oscillations. The corresponding carrier density n_{SdH} is 1.28 x 10^{13} cm^{-2}, derived from the

448 peak position of the Fourier transform as shown in the inset. **d**, Generation of a p-n

449 junction in BN/Gr/BN heterostructure by controlled e-beam exposure in lithography

450 mode. Temperature dependence of four-terminal resistance R versus V_G measured after
451 writing the p-n junction at 300 K. Inset shows the device geometry. The scale bar is 5
452 μm. **e,** Log scale plot of longitudinal four-terminal resistance R of the graphene p-n
453 junction as a function of magnetic field and gate voltage at 5 K. **f** and **g,** s-SNOM images
454 of a stripe pattern and a letter "B" pattern written in a BN/Gr/BN heterostructure using 2
455 keV e-beam at V_{SET} = 55 V. The scale bar is 2 μm in **f** and 1 μm in **g**. The spatial
456 resolution is about 200 nm indicated by the arrows in **g**.
457

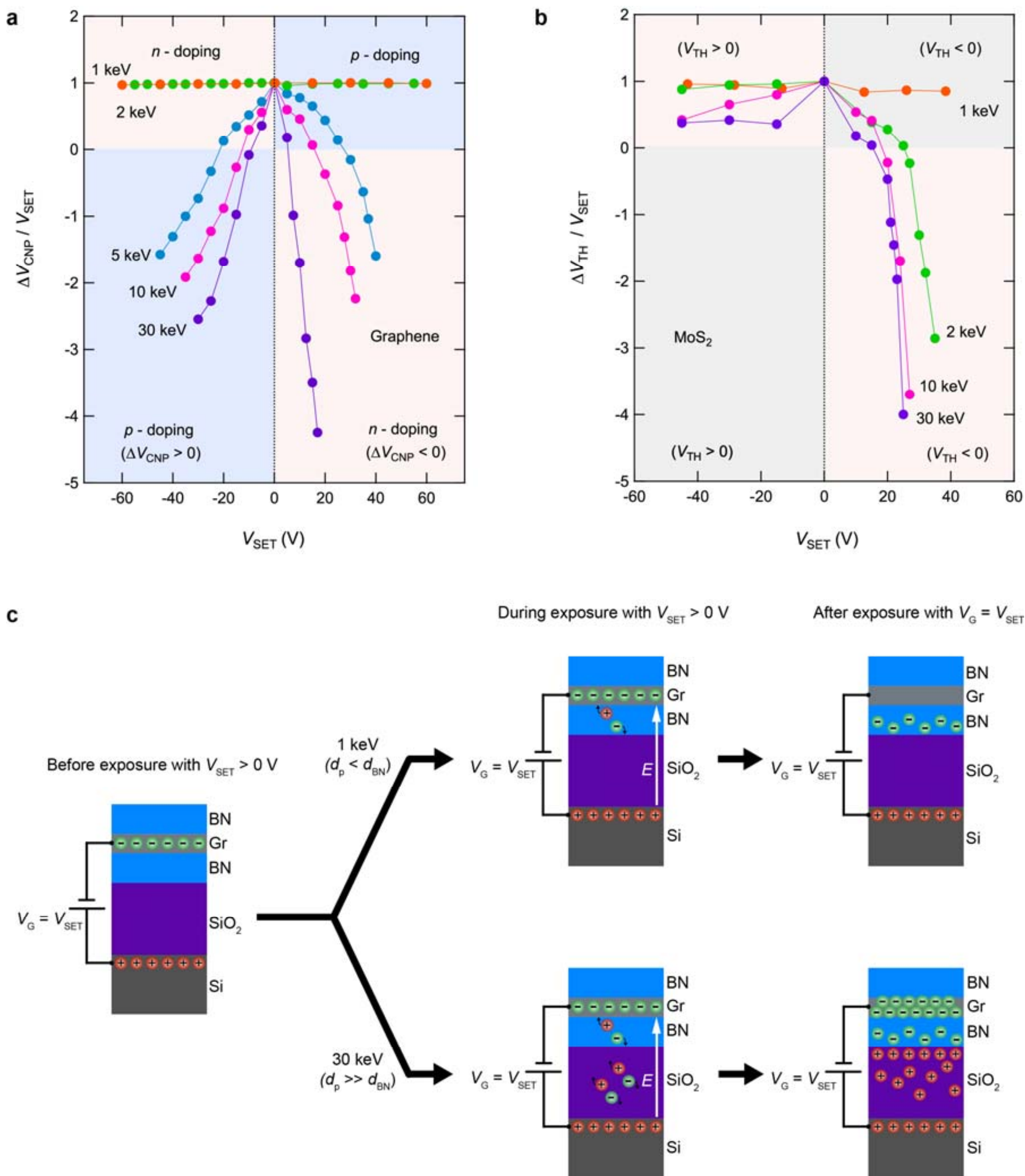

458

459 **Figure 4 | Energy dependence and proposed mechanism for e-beam induced doping**

460 **effect in graphene and MoS_2 vdW heterostructures. a**, Normalized effective

461 capacitance defined as $\Delta V_{CNP}/V_{SET}$ versus the corresponding V_{SET} for the e-beam doping

462 effect in graphene at different e-beam energies. Red and blue shaded regions indicate

463 electron and hole doping induced by e-beam exposure, respectively. **b**, Normalized

464 effective capacitance defined as $\Delta V_{TH}/V_{SET}$ versus V_{SET} for the e-beam doping effect in
465 ML MoS_2 at different e-beam energies. **c**, Schematic of the doping process and charge
466 carrier distribution for 1 keV and 30 keV e-beam doping in BN/Gr/BN at a positive V_{SET}.
467 Here, d_p is the penetration depth of the electron beam and d_{BN} is the total BN thickness.
468 In both scenarios, the device is kept at $V_G = V_{SET}$ after e-beam exposure. More detailed
469 schematic of the doping process is included in the SI (Supplementary Figs. S22 and S23).